

Towards the algorithmic treatment of 3D strong discontinuities

J. Mergheim[‡], E. Kuhl^{*,†} and P. Steinmann[§]

*Chair of Applied Mechanics, Department of Mechanical Engineering, University of Kaiserslautern,
P.O. Box 3049, 67653 Kaiserslautern, Germany*

SUMMARY

A geometrically non-linear finite element framework for the modelling of propagating discontinuities in three-dimensional continua is presented. By doubling the degrees of freedom in the discontinuous elements, the algorithm allows for arbitrary discontinuities which are not restricted to inter-element boundaries. The deformation field is interpolated independently on both sides of the discontinuity. In contrast to the X-FEM, the suggested approach thus relies exclusively on displacement degrees of freedom. On the discontinuity surface, the jump in the deformation is related to the cohesive tractions to account for smooth crack opening. Computational difficulties characteristic of three-dimensional crack propagation are addressed. The performance of the method is elaborated by means of a homogeneous three-dimensional tension problem and by means of the classical peel test. Copyright © 2006 John Wiley & Sons, Ltd.

Received 17 October 2005; Revised 13 April 2006; Accepted 24 April 2006

KEY WORDS: discontinuous elements; cohesive surfaces; propagating discontinuities; Nitsche's method

1. INTRODUCTION

The modelling of strong discontinuities within the finite element setting has gained increasing attention ever since the pioneering work on extended finite elements by Belytschko and Black [1], Moës *et al.* [2] and Sukumar *et al.* [3, 4]. The extended finite element method is extremely powerful and the underlying concept is remarkably simple: Enrichment functions are applied to interpolate a part of the deformation field which is decomposed in the standard continuous part and an additional discontinuous part. This discontinuous part is approximated independently by means of additional global degrees of freedom. As such, the extended finite element method is a particular instance of the partition of unity method, see Reference [5].

*Correspondence to: E. Kuhl, Chair of Applied Mechanics, Department of Mechanical Engineering, University of Kaiserslautern, P.O. Box 3049, 67653 Kaiserslautern, Germany.

[†]E-mail: ekuhl@rhrk.uni-kl.de

[‡]E-mail: mergheim@rhrk.uni-kl.de

[§]E-mail: ps@rhrk.uni-kl.de

Rather than following the classical X-FEM approach and introducing jumps in the deformation field as additional unknowns, we suggest a slightly modified approach based on the recent ideas by Hansbo and Hansbo [6, 7]. Their celebrated concept which essentially generalizes the ideas of Nitsche [8] was adopted by Mergheim *et al.* [9, 10] and is now being extended to finite deformations in a fully three-dimensional setting. In line with the Hansbo method, a discontinuous approximation is accomplished by doubling the degrees of freedom in the discontinuous elements, see also Reference [11]. Each of these two independent sets accounts for the interpolation of the deformation field on either side of the discontinuity surface. Two sets of the standard basis functions are used, one is put to zero on one side of the discontinuity while it takes its usual values on the other side and *vice versa*. This leads to a formulation which allows for an arbitrarily oriented discontinuity within an element, using only displacement degrees of freedom and the standard basis functions. As such, the Hansbo method proves particularly advantageous when treating degrees of freedom that are not additive such as directors in shell analysis as pointed out by Areias and Belytschko [12]. In contrast to the classical X-FEM, the Hansbo method is strictly local. Modifications affect only the discontinuous element itself and no additional transition elements are needed around the crack tip. Partially cracked elements, however, are more easily handled with the classical X-FEM approach by Belytschko and Black [1] and Mões *et al.* [2].

The two parts of the discontinuous element are held together by means of the cohesive crack concept. The essential idea of introducing an independent constitutive law relating interface tractions to displacement jumps was introduced by Dugdale [13] and Barenblatt [14] and has been used extensively in simulating the failure of quasi-brittle materials. In combination with the extended finite element method, it has been applied, e.g. by Wells *et al.* [15–17], Mões and Belytschko [18] and Gasser and Holzapfel [19].

This manuscript is organized as follows. In Section 2 we provide a brief summary of the governing equations for strong discontinuities. In Section 3 we then illustrate their finite element discretization. Details concerning the algorithmic realization are given in Section 4. In Section 5, two representative examples are presented before the paper closes with a final discussion in Section 6.

2. GOVERNING EQUATIONS OF STRONG DISCONTINUITIES

To set the stage, we shall briefly summarize the governing equations of strong discontinuities in the geometrically non-linear setting. Let \mathcal{B}_0 denote the material configuration occupied by the body of interest with material placements \mathbf{X} . The corresponding spatial configuration with placements \mathbf{x} is denoted by \mathcal{B} . Its boundary $\partial\mathcal{B}$ consists of disjoint parts $\partial\mathcal{B} = \partial\mathcal{B}_\varphi \cup \partial\mathcal{B}_t$ with $\partial\mathcal{B}_\varphi \cap \partial\mathcal{B}_t = \emptyset$ where either Dirichlet or Neumann boundary conditions are prescribed. By $\boldsymbol{\varphi}$ we shall denote the deformation mapping placements from the material to the spatial configuration $\mathbf{x} = \boldsymbol{\varphi}(\mathbf{X})$, cf. Figure 1. Elements of the corresponding tangent spaces are mapped by the deformation gradient $\mathbf{F} = \nabla_{\mathbf{X}}\boldsymbol{\varphi}$ as $d\mathbf{x} = \mathbf{F} \cdot d\mathbf{X}$. Let \mathcal{B}_0 be divided by a strong discontinuity Γ_0 with normal vector \mathbf{N} introducing the two subdomains \mathcal{B}_0^1 and \mathcal{B}_0^2 . Obviously $\boldsymbol{\varphi}$ and \mathbf{F} are continuous in either subdomain

$$\boldsymbol{\varphi}(\mathbf{X}) = \begin{cases} \boldsymbol{\varphi}^1(\mathbf{X}) & \text{in } \mathcal{B}^1, \\ \boldsymbol{\varphi}^2(\mathbf{X}) & \text{in } \mathcal{B}^2, \end{cases} \quad \mathbf{F} = \begin{cases} \mathbf{F}^1 = \nabla_{\mathbf{X}}\boldsymbol{\varphi}^1 & \text{in } \mathcal{B}^1 \\ \mathbf{F}^2 = \nabla_{\mathbf{X}}\boldsymbol{\varphi}^2 & \text{in } \mathcal{B}^2 \end{cases} \quad (1)$$

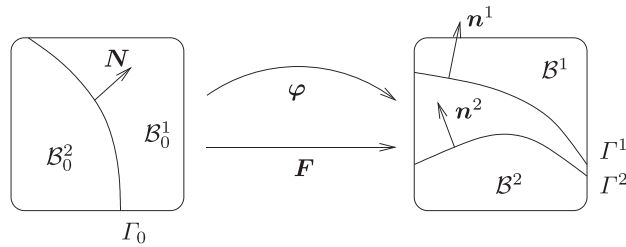


Figure 1. Kinematics—strong discontinuities.

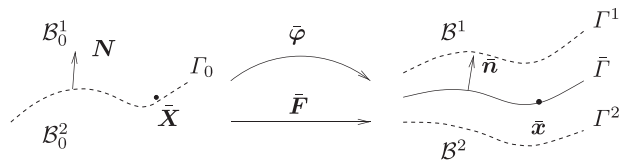


Figure 2. Kinematics—fictitious discontinuity surface in the spatial configuration.

but non-continuous across the discontinuity surface. For each subdomain \mathcal{B}_0^α we thus introduce an independent field of Jacobians $J^\alpha = \det(\mathbf{F}^\alpha)$ and of characteristic strain measures, e.g. the field of left Cauchy–Green tensors $\mathbf{b}^\alpha = \mathbf{F}^\alpha \cdot \mathbf{F}^{\alpha t}$ with $\alpha = 1, 2$. On the discontinuity surface Γ_0 , the deformation field $\boldsymbol{\varphi}$ is obviously non-unique. Its jump $[[\boldsymbol{\varphi}]]$ can be expressed in the following form:

$$[[\boldsymbol{\varphi}]] = \boldsymbol{\varphi}^1 - \boldsymbol{\varphi}^2 \quad \text{on } \bar{\Gamma}, \quad \bar{\mathbf{F}} = 0.5[\mathbf{F}^1 + \mathbf{F}^2] \quad \text{on } \bar{\Gamma} \quad (2)$$

Recall that due to the discontinuity in the deformation map $\boldsymbol{\varphi}$ the unique discontinuity surface Γ_0 is mapped onto the surfaces Γ^1 and Γ^2 . We thus define a fictitious discontinuity surface $\bar{\Gamma}$ in the current configuration which can be identified through the average deformation map $\bar{\boldsymbol{\varphi}} = 0.5[\boldsymbol{\varphi}^1 + \boldsymbol{\varphi}^2]$, its related deformation gradient $\bar{\mathbf{F}}$ and the Jacobian $\bar{J} = \det(\bar{\mathbf{F}})$, cf. Figure 2. Next, we have to define appropriate constitutive equations for the bulk stress $\boldsymbol{\sigma}$ and for the cohesive tractions $\bar{\mathbf{t}}$. In what follows, we shall assume that the Cauchy stress in the bulk

$$\boldsymbol{\sigma}(\mathbf{F}) = \begin{cases} \boldsymbol{\sigma}(\mathbf{F}^1) & \text{in } \mathcal{B}^1 \\ \boldsymbol{\sigma}(\mathbf{F}^2) & \text{in } \mathcal{B}^2 \end{cases} \quad (3)$$

obeys a Neo-Hooke type constitutive law with $\boldsymbol{\sigma}(\mathbf{F}^\alpha) = [\lambda \ln(J^\alpha)\mathbf{I} - \mu\mathbf{I} + \mu\mathbf{b}^\alpha]/J^\alpha$ on either side \mathcal{B}^α of the discontinuity with $\alpha = 1, 2$. The inelastic behaviour is attributed exclusively to the discontinuity surface for which we introduce a constitutive law of the following form:

$$\bar{\mathbf{t}} = \bar{\mathbf{t}}_n([[\boldsymbol{\varphi}_n]]) + \bar{\mathbf{t}}_m([[\boldsymbol{\varphi}_m]]) \quad \text{on } \bar{\Gamma} \quad (4)$$

For the sake of simplicity, we have adopted an uncoupled traction separation law for which the normal traction vector $\bar{\mathbf{t}}_n([[\boldsymbol{\varphi}_n]])$ is expressed only in terms of normal jump vector $[[\boldsymbol{\varphi}_n]]) = [[\boldsymbol{\varphi}]]) \cdot \mathbf{n}$, e.g. as $\bar{\mathbf{t}}_n = f_t \exp(-f_t/G_f [[\boldsymbol{\varphi}]]) \cdot \mathbf{n}$. Here, f_t denotes the tensile strength and G_f is the fracture

energy. Similarly, the in-plane traction vector $\bar{\mathbf{t}}_m(\llbracket \boldsymbol{\varphi}_m \rrbracket)$ is assumed to be a function of the tangential jump $\llbracket \boldsymbol{\varphi}_m \rrbracket = \llbracket \boldsymbol{\varphi} \rrbracket - \llbracket \boldsymbol{\varphi}_n \rrbracket$ alone, e.g. in its most simple linear form as $\bar{\mathbf{t}}_m = d \llbracket \boldsymbol{\varphi}_m \rrbracket$ in terms of the shear stiffness d . The weak formulation of the governing equations, i.e. the equilibrium equation in \mathcal{B}_0 , the Neumann boundary conditions on $\partial \mathcal{B}_{0t}$ and the traction continuity equation along Γ_0 , follows straightforwardly from the multiplication with the vector valued test function $\delta \boldsymbol{\varphi}$, the integration over the corresponding domains and some standard algebraic transformations. Its push forward to the spatial configuration renders the following expression:

$$\int_{\mathcal{B}^1 \cup \mathcal{B}^2} \nabla_{\mathbf{x}} \delta \boldsymbol{\varphi} : \boldsymbol{\sigma} \, dv + \int_{\bar{\Gamma}} \llbracket \delta \boldsymbol{\varphi} \rrbracket \cdot \bar{\mathbf{t}} \, d\bar{a} - \int_{\partial \mathcal{B}_t} \delta \boldsymbol{\varphi} \cdot \mathbf{t}^p \, da = 0 \quad (5)$$

in terms of the true stresses $\boldsymbol{\sigma}$, the true cohesive tractions $\bar{\mathbf{t}}$ and the push forward of the prescribed surface tractions \mathbf{t}^p , see, e.g. Mergheim *et al.* [9, 10].

3. DISCRETIZATION OF STRONG DISCONTINUITIES

In the present section, we illustrate the numerical discretization of the weak form (5) with the help of the finite element method in the sense of Hansbo and Hansbo [7]. In the spirit of the finite element method, the domain of interest \mathcal{B} is divided into n_{el} elements. It proves convenient to distinguish between the standard continuous elements \mathcal{B}_c and the discontinuous elements \mathcal{B}_d which are intersected by the discontinuity surface. In the continuous elements, the deformation map $\boldsymbol{\varphi}$ and its spatial gradient \mathbf{F} take the classical elementwise representation

$$\boldsymbol{\varphi}|_{\mathcal{B}_c} = \sum_{i=1}^{n_{\text{en}}} N^i \boldsymbol{\varphi}_i, \quad \mathbf{F}|_{\mathcal{B}_c} = \sum_{i=1}^{n_{\text{en}}} \boldsymbol{\varphi}_i \otimes \nabla_{\mathbf{X}} N^i \quad (6)$$

with N^i denoting the standard shape functions for tetrahedral elements and n_{en} being the number of element nodes. For the discontinuous elements, $\boldsymbol{\varphi}^1$ and its gradient \mathbf{F}^1 are only defined in \mathcal{B}_d^1 , however, they are approximated by the nodal values at all element nodes in terms of the standard basis functions. The same applies to $\boldsymbol{\varphi}^2$ and \mathbf{F}^2 in \mathcal{B}_d^2 which have no relation to $\boldsymbol{\varphi}^1$ and \mathbf{F}^1 as indicated by Equation (1)

$$\boldsymbol{\varphi}|_{\mathcal{B}_d^\alpha} = \sum_{i=1}^{n_{\text{en}}} N^{\alpha i} \boldsymbol{\varphi}_{\alpha i}, \quad \mathbf{F}|_{\mathcal{B}_d^\alpha} = \sum_{i=1}^{n_{\text{en}}} \boldsymbol{\varphi}_{\alpha i} \otimes \nabla_{\mathbf{X}} N^{\alpha i} \quad (7)$$

With $\alpha = 1, 2$ for either side of the discontinuity, $\boldsymbol{\varphi}_{\alpha i}$ are the nodal values of the deformation map belonging to \mathcal{B}_d^1 and \mathcal{B}_d^2 , respectively, represented by the element nodes $i = 1, \dots, n_{\text{en}}$. We thus apply two copies of the standard basis functions. One set is put to zero on one side of the discontinuity, while it takes its usual values on the other side, and *vice versa*, i.e. $N^{\alpha i} = N^i$ in \mathcal{B}_d^α and $N^{\alpha i} = 0$ otherwise. As pointed out recently by Areias and Belytschko [12], these basis functions $N^{\alpha i}$ of the Hansbo method are in fact nothing but linear combinations of the standard X-FEM basis. According to Equation (2), the jump in the deformation map $\llbracket \boldsymbol{\varphi} \rrbracket$ is described as the difference of the two continuous fields at the internal boundary $\bar{\Gamma}$. Its average gradient introduces the deformation gradient $\bar{\mathbf{F}}$ on the fictitious discontinuity surface $\bar{\Gamma}$

$$\llbracket \boldsymbol{\varphi} \rrbracket|_{\bar{\Gamma}} = \sum_{p=1}^{n_{\text{en}} + n_{\text{en}}^*} M^p \boldsymbol{\varphi}_p, \quad \bar{\mathbf{F}}|_{\bar{\Gamma}} = \sum_{p=1}^{n_{\text{en}} + n_{\text{en}}^*} \boldsymbol{\varphi}_p \otimes \mathbf{L}^p \quad (8)$$

The newly introduced set M comprises the standard shape functions N^α , evaluated at $\bar{\Gamma}$ equipped with the corresponding plus or minus sign in order to represent the jump terms. The set \mathbf{L} contains the gradients of the shape functions evaluated at $\bar{\Gamma}$ and the averaging factor 0.5. Recall that in contrast to the extended finite element method, the jump in the deformation map is not treated as an explicit variable. Rather, the approximation of the jump term arises automatically from the independent approximation of the deformation maps. With the discretizations (6)–(8), the weak form (5) can be cast into the following discrete residual statement:

$$\mathbf{R}^I = \mathbf{A}_{c,d=1}^{nel} \int_{\mathcal{B}_c} \nabla_{\mathbf{x}} N^i \cdot \boldsymbol{\sigma} \, dv + \int_{\mathcal{B}_d^z} \nabla_{\mathbf{x}} N^{\alpha i} \cdot \boldsymbol{\sigma} \, dv + \int_{\bar{\Gamma}_d} M^i \bar{\mathbf{t}} \, d\bar{a} - \int_{\partial \mathcal{B}_t} N^i \mathbf{t}^p \, da = \mathbf{0} \quad (9)$$

where $\mathbf{A}_{c,d=1}^{nel}$ denotes the assembly of all element contributions, the standard continuous and the discontinuous ones, at the element nodes $i = 1, \dots, n_{en} + n_{en}^*$, including the newly introduced ones n_{en}^* , to the overall residuum at the global node points $I = 1, \dots, n_{np} + n_{np}^*$. For the solution of the non-linear equation (9), we suggest an incremental iterative Newton–Raphson scheme based on the consistent linearization $\mathbf{R}_{k+1}^I = \mathbf{R}_k^I + d\mathbf{R}^I = \mathbf{0}$ with $d\mathbf{R}^I = \sum_{J=1}^{n_{np} + n_{np}^*} \mathbf{K}^{IJ} d\boldsymbol{\varphi}^J$. Accordingly, the global tangent stiffness matrix $\mathbf{K}^{IJ} = \partial \mathbf{R}^I / \partial \boldsymbol{\varphi}^J$ takes the following explicit representation:

$$\begin{aligned} \mathbf{K}^{IJ} = & \mathbf{A}_{c,d=1}^{nel} \int_{\mathcal{B}_c} \nabla_{\mathbf{x}} N^i \cdot \mathbf{e} \cdot \nabla_{\mathbf{x}} N^j \, dv + \int_{\mathcal{B}_c} \nabla_{\mathbf{x}} N^i \cdot \boldsymbol{\sigma} \cdot \nabla_{\mathbf{x}} N^j \mathbf{I} \, dv \\ & + \int_{\mathcal{B}_d^z} \nabla_{\mathbf{x}} N^{\alpha i} \cdot \mathbf{e} \cdot \nabla_{\mathbf{x}} N^{\alpha j} \, dv + \int_{\mathcal{B}_d^z} \nabla_{\mathbf{x}} N^{\alpha i} \cdot \boldsymbol{\sigma} \cdot \nabla_{\mathbf{x}} N^{\alpha j} \mathbf{I} \, dv \\ & + \int_{\bar{\Gamma}_d} M^i \bar{\mathbf{T}}_\varphi M^j \, d\bar{a} + \int_{\bar{\Gamma}_d} M^i \bar{\mathbf{T}}_n \cdot \bar{\mathbf{n}}_F \cdot \mathbf{L}^j \, d\bar{a} + \int_{\bar{\Gamma}_d} M^i \bar{\mathbf{t}} [\bar{\mathbf{A}} \cdot \mathbf{L}^j] \, d\bar{a} \end{aligned} \quad (10)$$

The fourth-order tensor \mathbf{e} contains the classical elastic tangent moduli which follow straight forwardly from the linearization of the Cauchy stress as $\mathbf{e} = [\lambda \mathbf{I} \otimes \mathbf{I} + 2[\mu - \lambda \ln(J)] \bar{\mathbf{i}}] / J$ with $\bar{\mathbf{i}}$ denoting the symmetric spatial fourth-order identity. Moreover, we have introduced the second-order tensors $\bar{\mathbf{T}}_\varphi$ and $\bar{\mathbf{T}}_n$ containing the directional derivative of the cohesive traction $\bar{\mathbf{t}}$ with respect to the jump $[[\boldsymbol{\varphi}]]$ and the normal vector $\bar{\mathbf{n}}$. The second-order tensor $\bar{\mathbf{A}}$ is $\bar{\mathbf{A}} = [\mathbf{I} - \bar{\mathbf{n}} \otimes \bar{\mathbf{n}}] \cdot \bar{\mathbf{F}}^{-1}$ and the third-order tensor $\bar{\mathbf{n}}_F$ characterizes the derivative of the normal vector $\bar{\mathbf{n}}$ with respect to the deformation gradient $\bar{\mathbf{F}}$.

$$\begin{aligned} \bar{\mathbf{T}}_\varphi &= \frac{\partial \bar{\mathbf{t}}}{\partial [[\boldsymbol{\varphi}]]} = \frac{\partial \bar{\mathbf{t}}}{\partial [[\boldsymbol{\varphi}_n]]} \cdot [\bar{\mathbf{n}} \otimes \bar{\mathbf{n}}] + \frac{\partial \bar{\mathbf{t}}}{\partial [[\boldsymbol{\varphi}_m]]} \cdot [\mathbf{I} - \bar{\mathbf{n}} \otimes \bar{\mathbf{n}}] \\ \bar{\mathbf{T}}_n &= \frac{\partial \bar{\mathbf{t}}}{\partial \bar{\mathbf{n}}} = \frac{\partial \bar{\mathbf{t}}}{\partial [[\boldsymbol{\varphi}_n]]} \cdot [\bar{\mathbf{n}} \otimes [[\boldsymbol{\varphi}]] + [[[\boldsymbol{\varphi}]] \cdot \bar{\mathbf{n}}] \mathbf{I}] - \frac{\partial \bar{\mathbf{t}}}{\partial [[\boldsymbol{\varphi}_m]]} \cdot [\bar{\mathbf{n}} \otimes [[\boldsymbol{\varphi}]] + [[[\boldsymbol{\varphi}]] \cdot \bar{\mathbf{n}}] \mathbf{I}] \\ \bar{\mathbf{n}}_F &= \frac{\partial \bar{\mathbf{n}}}{\partial \bar{\mathbf{F}}} = -\bar{\mathbf{n}} \cdot [\mathbf{I} \otimes \bar{\mathbf{F}}^{-1}] + \bar{\mathbf{n}} \otimes \bar{\mathbf{n}} \otimes \bar{\mathbf{n}} \cdot \bar{\mathbf{F}}^{-1} \end{aligned} \quad (11)$$

In the above expressions, $\bar{\mathbf{n}} = \bar{\mathbf{n}}^* / |\bar{\mathbf{n}}^*|$ is the spatial unit normal with $\bar{\mathbf{n}}^* = \mathbf{N} \cdot \bar{\mathbf{F}}^{-1}$ and $\bar{\otimes}$ denotes the non-standard dyadic product according to the following componentwise representation $\{\bullet \bar{\otimes} \circ\}_{ijkl} = \{\bullet\}_{ik} \otimes \{\circ\}_{jl}$.

4. ALGORITHMIC TREATMENT OF STRONG DISCONTINUITIES

In what follows, we will give a brief illustration of the algorithmic treatment of strong discontinuities in the three-dimensional setting and refer to Sukumar *et al.* [3], Gasser and Holzapfel [19] and Areias and Belytschko [20] for more sophisticated details. For the sake of simplicity we apply linear tetrahedral elements, the discontinuity surface is assumed to be flat within an element and immediately intersects the entire element upon initiation.

4.1. Discontinuous elements

Unlike linear triangles, linear tetrahedra can be intersected by the discontinuity in two different ways. If the discontinuity surface cuts three edges of the element such that the element interface becomes triangular, one tetrahedral element and one wedge element with two triangular and three quadrilateral faces are generated, see Figure 3, left. Alternatively, the discontinuity surface could intersect four edges of the element generating a quadrilateral interface as illustrated in Figure 3, right. In this case, the resulting subelements are both polyhedral wedge elements consisting of two triangular and three quadrilateral faces.

4.2. Numerical integration

Once the global and local co-ordinates \mathbf{X} and ξ of the three or four intersection points have been determined, the numerical integration over the discontinuous elements does not pose additional difficulties in general. In order to restrict ourselves to one single type of elements, we suggest to further subdivide each generated wedge element into three subtetrahedra. In total, the discontinuous element is thus subdivided in four or six subtetrahedra depending on the shape of the element interface. Their integration points ξ are then simply given by the centres of gravity of the individual subtetrahedra. The typical integration of a function $g(\mathbf{X})$ over a discontinuous element \mathcal{B}_d thus takes the following representation:

$$\int_{\mathcal{B}_d} g(\mathbf{X}) dV = \sum_{i=1}^{n_{ip}^+} g^+(\xi_i) \det(\mathbf{J}(\xi_i)) \omega_i + \sum_{j=1}^{n_{ip}^-} g^-(\xi_j) \det(\mathbf{J}(\xi_j)) \omega_j$$

whereby $n_{ip}^{+,-}$ is the number of integration points and ω are the associated weighting factors.

In addition to this volume integration, the integration of the cohesive tractions has to be carried out over the intersection plane. This requires the evaluation of a surface integral over either

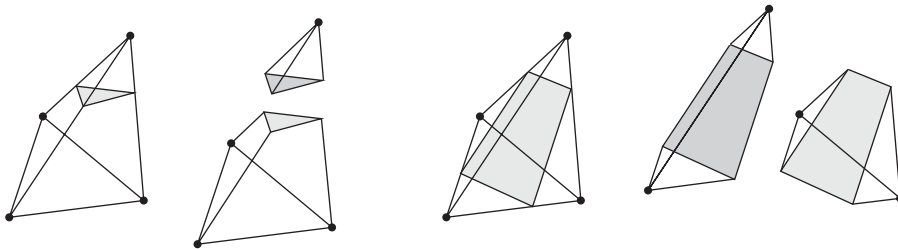


Figure 3. Discontinuous elements—two different sets of subelements of discontinuous tetrahedron.

a triangular or a quadrilateral discontinuity surface. To this end, an additional co-ordinate transformation from the global co-ordinates \mathbf{X} to the two-dimensional local co-ordinates of the intersection surface $\zeta = [\zeta_1, \zeta_2]^t$ is introduced. Incremental line elements $d\mathbf{X}$ and incremental surface elements dA can then be expressed in terms of the local co-ordinates ζ as

$$d\mathbf{X} = \mathbf{J}_\zeta \cdot d\zeta, \quad dA = \left\| \begin{bmatrix} J_{\zeta 11} \\ J_{\zeta 21} \\ J_{\zeta 31} \end{bmatrix} \times \begin{bmatrix} J_{\zeta 12} \\ J_{\zeta 22} \\ J_{\zeta 32} \end{bmatrix} \right\| d\zeta_1 d\zeta_2$$

whereby the non-square Jacobian $\mathbf{J}_\zeta = \partial\mathbf{X}/\partial\zeta$ contains the partial derivatives of the global three-dimensional co-ordinates \mathbf{X} with respect to the local surface co-ordinates ζ . Again, in order to restrict ourselves to one single element type, we suggest to apply either one or two triangular elements with three integration points for the integration over the intersection plane.

4.3. Crack propagation and crack path representation

We suggest a classical failure criterion of Rankine type to govern crack propagation and refer to the literature for more advanced failure initiation criteria, see, e.g. Fagerström and Larsson [21] or Mergheim [10]. If the principal stress in the elements ahead of the crack-tip exceeds the tensile strength of the material, the discontinuity is elongated and the corresponding element is inserted into the *set of discontinuous elements*. In addition, we store the crack surface represented by the triangular or quadrilateral intersection plane characterized through its normal vector and a point lying on the surface. The faces between discontinuous and continuous elements constitute the *set of crack-tip faces*. The failure criterion is checked for all elements that border a crack-tip face. If the failure criterion is met, the set of discontinuous elements and the set of crack-tip faces have to be updated. Furthermore, the new degrees of freedom have to be introduced. The load step is recalculated with the modified geometry and the crack criterion is controlled for the new set of elements next to the crack-tip faces. The procedure is repeated until no further element failure is observed.

One major constraint in the present three-dimensional formulation is that the crack geometry is restricted to planar cracks. Accordingly, in the reference configuration, the normal vector to the crack plane is identical in each element. Nevertheless, this is not a general limitation of the method as such but rather an assumption that is made to simplify the geometrical representation of the crack surface and the crack propagation. In the special case of planar crack propagation, crack path continuity is *a priori* ensured. If non-planar crack growth is considered the crack path becomes either discontinuous as in Reference [19], or the normal vector of the crack surface in one element has to be influenced by the neighbouring ones to ensure crack path continuity [20].

4.4. Algorithmic implementation

The decisive differences of the present approach to a standard finite element code is the introduction of discontinuous elements. Nevertheless, the necessary modifications can easily be realized even in commercial codes. Since the discontinuous elements consist of two continuous subelements with modified integration regions, the element routine for discontinuous elements has to be altered only little. The shape functions and the number of degrees of freedom for each subelement are as usual. The implementation of the discontinuous elements requires a routine to store the cracked elements

Table I. Algorithmic implementation.

```

repeat
  global Newton iteration
  loop over all continuous elements  $\mathcal{B}_c$ 
    calculation of element residua  $\mathbf{R}_c^{\text{int}}$  and their derivatives  $\mathbf{K}_c^{\text{int}}$ 
  loop over all discontinuous elements  $\mathcal{B}_d$ 
    loop over all element subdomains
      calculation of element residua and their derivatives
    assembly of  $\mathbf{R}_d^{\text{int}}$  and  $\mathbf{K}_d^{\text{int}}$ 
      calculation of the surface contributions  $\mathbf{R}_d^{\text{coh}}$  and  $\mathbf{K}_d^{\text{coh}}$ 
    assembly of global residual  $\mathbf{R}$  and tangent stiffness  $\mathbf{K}$ 
  solution of equilibrium equation, calculation of nodal deformation map  $\boldsymbol{\varphi}$ 
  check failure criterion for elements next to crack tip faces, if crack is unstable  $\sigma_I > f_t$ 
    introduction of new degrees of freedom
    determination of intersection points and geometry in discontinuous element
    update of sets of discontinuous elements and crack tip faces
until crack geometry is stable  $\sigma_I < f_t$ 

```

and to decide whether the usual *continuous element function* or the *discontinuous element function* has to be called. In the considered case of cohesive cracks, yet an additional subroutine for the calculation of the surface tractions is required.

The implementation of the crack propagation entails additional post-processing steps, including the introduction of the new degrees of freedom and the determination of the geometry of the discontinuous elements. When an element is identified to crack, firstly the new degrees of freedom are introduced. Then, the set of discontinuous elements and the set of crack tip faces are updated. For each discontinuous element, the intersection points and the geometry of the element parts are stored since they do not change during the simulation. To decide which elements are connected to the crack tip faces not only the usual element connectivity has to be provided but also the face connectivity. The connectivity tables can be calculated and stored once in the beginning of the calculation. The general steps of the numerical implementation for one load step are summarized in Table I.

5. EXAMPLES

We elaborate two different examples, a homogeneous rectangular block under tension and a three-dimensional version of the classical peel test. The results of different discretizations are compared to analyse the convergence of the method.

5.1. Tensile test

The first example is a simple mode I failure problem of a rectangular block subjected to tensile loading. The block is fixed on one side and loaded by a prescribed displacement on the other side. Failure is initialized on two lateral faces of the specimen, as indicated in Figure 4. The material parameters are chosen as $\lambda = 3846 \text{ N/mm}^2$, $\mu = 3846 \text{ N/mm}^2$, $f_t = 200 \text{ N/mm}^2$ and $G_f = 100 \text{ N/mm}$. The block has a square cross section of 1 mm^2 and is 2 mm high.

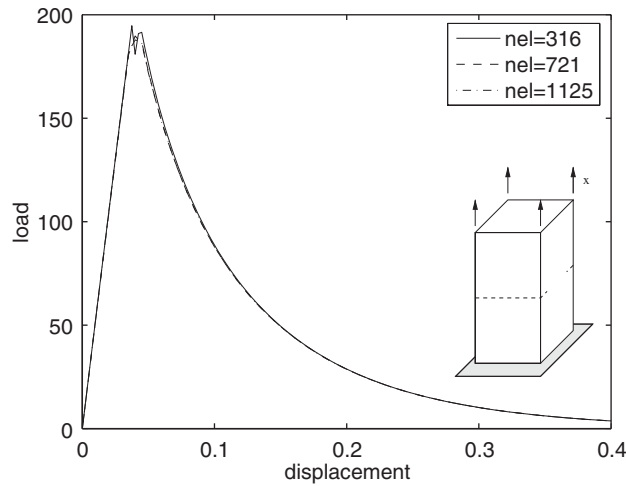


Figure 4. Tension test—load displacement relation.

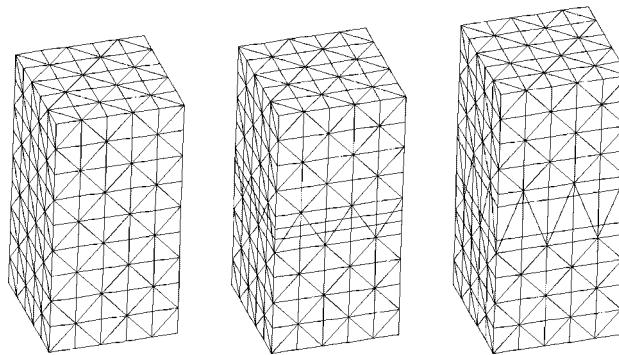


Figure 5. Tensile test—deformation of block at different load steps.

In order to analyse the mesh sensitivity of the algorithm, the computation is carried out with three different meshes, containing 316, 720 and 1125 elements. When the critical stress state is reached, the crack propagates through the specimen with a straight horizontal path. The complete separation of the two parts of the block is prevented by the cohesive traction. The deformation of the block with 1125 elements is shown in Figure 5. The first figure corresponds to the pre-critical state with an applied displacement of 0.04 mm. The two other figures show post-critical deformation states at prescribed displacements of 0.2 and 0.4 mm.

In Figure 5 the separation of the two sides of the discontinuity surface is indicated by plotting the intersection planes in addition to the usual elements. It is visible that the opening increases significantly. The expected exponential unloading with an increasing opening can be verified by the load displacement diagram in Figure 4. As expected an initially elastic behaviour can be observed.

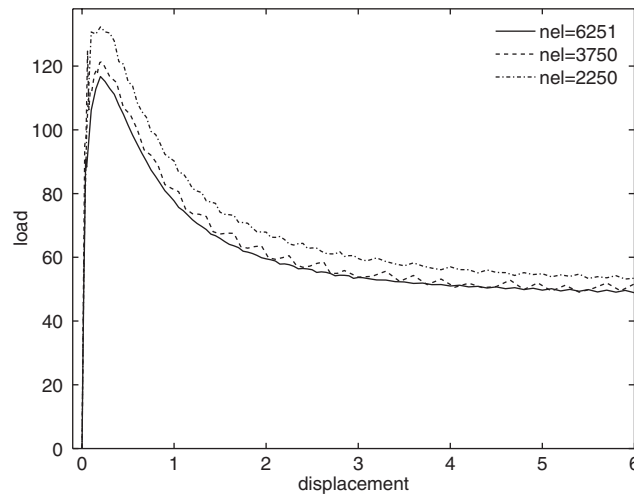


Figure 6. Peel test—load displacement relation.

When the critical stress state is reached the load drops down rapidly and decreases exponentially with the opening.

The global load displacement response is given for the three different discretizations. It is obvious that the solutions are independent of the underlying discretization. The curve of the coarsest mesh shows slight oscillations in the post-critical regime. As reported by Simone *et al.* [22], these oscillations can be attributed to the discretization error in the post-processed stresses which enter the failure criterion. Nevertheless, the spurious oscillations are already smoothed out for the second mesh with 712 elements.

5.2. Peel test

A typical benchmark problem for discontinuous failure is the classical symmetric peel test as elaborated intensively, e.g. by Wells *et al.* [16, 17]. Herein, we elaborate its extension to the three-dimensional setting. A cantilever beam is fixed on one side and a displacement is prescribed on the upper and lower edge on the other end of the beam where a crack is initialized at half of the beam height. The material parameters are chosen as $\lambda = 2778 \text{ N/mm}^2$, $\mu = 4167 \text{ N/mm}^2$, $f_t = 200 \text{ N/mm}^2$ and $G_f = 100 \text{ N/mm}$ and the tangential stiffness d is set to zero. The beam is 10mm long and has an initial square cross section of 1 mm^2 . To avoid penetration of the cohesive zone an additional penalty constraint is added to the weak form. The computations are accomplished with three different meshes with 2250, 3750 and 6250 linear tetrahedral elements. The displacement is prescribed in 100 increments up to a final opening of 12 mm. Since the specimen is fixed on the left-hand side, the total separation of the two layers is prevented. The deformation of the structure at different loading stages is pictured in Figure 7. The response is symmetric and the discontinuity propagates along the centre line but is not aligned with the element boundaries.

The load displacement response for the three different discretizations is plotted in Figure 6. It clearly reveals the characteristic features of the peel test and qualitatively agrees nicely with the two-dimensional simulations documented by Wells *et al.* [16, 17]. The curve for the coarse

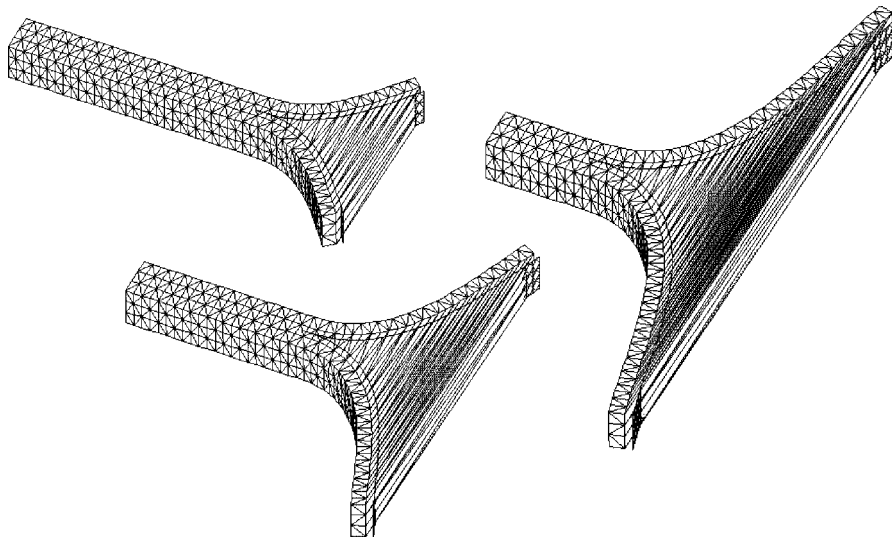


Figure 7. Peel test—deformation of the structure at different stages of loading.

discretization is quite different from the ones of the finer meshes. The maximum reaction force is overestimated and also the post peak behaviour shows minor differences. For the coarsest mesh, the elements are too large to approximate the high stress gradients correctly. The stresses entering the failure criterion are underestimated and failure occurs later in larger elements. In general, the discretization with only 2250 elements is not sufficient. Its load displacement curve even shows slight oscillations which can be attributed to the elementwise failure. However, these oscillations are smoothed out for the sufficiently fine discretization with 6250 elements. As the computations for the finer discretizations are in good agreement, the method can with no doubt be classified as producing mesh independent results in the sense of mesh refinement.

6. DISCUSSION

A computational strategy for the simulation of propagating discontinuities in three-dimensional continua was introduced. Its essential feature are discontinuous finite elements in which the deformation field is continuous on either side of the discontinuity surface but exhibits a jump across it. The number of degrees of freedom in these elements is doubled and the deformation is interpolated independently on both sides of the discontinuity. Smooth crack opening is ensured through the cohesive crack concept introducing cohesive tractions which decrease upon increased crack opening. Particular attention was attributed to the three-dimensional algorithmic treatment which faces additional difficulties as compared to the two-dimensional framework. A homogeneous tension problem and the classical symmetric peel test have been analysed to illustrate the basic features of the suggested approach. Similar to the celebrated extended finite element method, the crack path is independent of the underlying finite element mesh. While the X-FEM requires additional transition elements, our modifications are strictly local and only affect the discontinuous

elements themselves. The suggested method is thus believed to be extremely powerful in simulating propagating discontinuities not only in two but also in three-dimensional continua. Its extension to non-planar crack propagation is part of current research.

REFERENCES

1. Belytschko T, Black T. Elastic crack growth in finite elements with minimal remeshing. *International Journal for Numerical Methods in Engineering* 1999; **45**:601–620.
2. Moës N, Dolbow J, Belytschko T. A finite element method for crack growth without remeshing. *International Journal for Numerical Methods in Engineering* 1999; **46**:131–150.
3. Sukumar N, Moës N, Moran B, Belytschko T. Extended finite element method for three-dimensional crack modeling. *International Journal for Numerical Methods in Engineering* 2000; **48**(11):1549–1570.
4. Sukumar N, Chopp DL, Moës N, Belytschko T. Modeling holes and inclusions by level sets in the extended finite-element method. *Computer Methods in Applied Mechanics and Engineering* 2001; **190**:6183–6200.
5. Babuška I, Melenk JM. The partition of unity method. *International Journal for Numerical Methods in Engineering* 1997; **40**:727–758.
6. Hansbo A, Hansbo P. An unfitted finite element method, based on Nitsche's method, for elliptic interface problems. *Computer Methods in Applied Mechanics and Engineering* 2002; **191**:5537–5552.
7. Hansbo A, Hansbo P. A finite element method for the simulation of strong and weak discontinuities in solid mechanics. *Computer Methods in Applied Mechanics and Engineering* 2004; **193**:3523–3540.
8. Nitsche J. Über ein Variationsprinzip zur Lösung von Dirichlet-Problemen bei Verwendung von Teilräumen, die keinen Randbedingungen unterworfen sind. *Abh. Math. Univ. Hamburg* 1970; **36**:9–15.
9. Mergheim J, Kuhl E, Steinmann P. A finite element method for the computational modelling of cohesive cracks. *International Journal for Numerical Methods in Engineering* 2005; **63**(2):276–289.
10. Mergheim J. Computational modeling of strong and weak discontinuities. *Ph.D. Thesis*. TU Kaiserslautern, Germany, 2005.
11. Hansbo P. Nitsche's method for interface problems in computational mechanics. *GAMM Mitteilungen* 2005; **28**:183–206.
12. Areias PMA, Belytschko T. Letter to the Editor: A review on the article 'A finite element method for the simulation of strong and weak discontinuities in solid mechanics'. *Computer Methods in Applied Mechanics and Engineering* 2006; **195**:1275–1276.
13. Dugdale DS. Yielding of steel sheets containing slits. *Journal of Mechanics and Solids* 1960; **8**:100–108.
14. Barenblatt GI. The mathematical theory of equilibrium of cracks in brittle fracture. *Advances in Applied Mechanics* 1962; **7**:55–129.
15. Wells GN, Sluys LJ. A new method for modelling cohesive cracks using finite elements. *International Journal for Numerical Methods in Engineering* 2001; **50**:2667–2682.
16. Wells GN, Sluys LJ, de Borst R. A consistent geometrically non-linear approach for delamination. *International Journal for Numerical Methods in Engineering* 2002; **54**:1333–1355.
17. Wells GN. Dislocation modelling of strain localization and failure. *Ph.D. Thesis*. TU Delft. The Netherlands, 2001.
18. Moës N, Belytschko T. Extended finite element method for cohesive crack growth. *Engineering Fracture Mechanics* 2002; **69**(7):813–833.
19. Gasser TC, Holzapfel GA. Modeling 3d crack propagation in unreinforced concrete using pufem. *Computer Methods in Applied Mechanics and Engineering* 2005; **194**:2859–2896.
20. Areias PMA, Belytschko T. Analysis of three-dimensional crack initiation and propagation using the extended finite element method. *International Journal for Numerical Methods in Engineering* 2005; **63**:760–788.
21. Fagerström M, Larsson R. Theory and numerics for finite deformation fracture modelling using strong discontinuities. *International Journal for Numerical Methods in Engineering* 2006, submitted for publication.
22. Simone A, Wells GN, Sluys LJ. From continuous to discontinuous failure in a gradient-enhanced continuum damage model. *Computer Methods in Applied Mechanics and Engineering* 2003; **192**:4581–4607.
23. Gasser TC, Holzapfel GA. Geometrically non-linear and consistently linearized embedded strong discontinuity models for 3d problems with an application to the dissection analysis of soft biological tissues. *Computer Methods in Applied Mechanics and Engineering* 2003; **192**:5059–5098.